Spatially resolved spectroscopy of the E+A galaxies in the $z = 0.32$ cluster AC 114

Michael B. Pracy,[1]★ Warrick J. Couch,[1] Chris Blake,[1,2] Kenji Bekki,[1] Craig Harrison,[3] Matthew Colless,[4] Harald Kuntschner[5] and Roberto de Propris[6]

[1]*School of Physics, University of New South Wales, Sydney, NSW 2052, Australia*
[2]*Department of Physics & Astronomy, University of British Columbia, 6224 Agricultural Road, Vancouver, BC, V6T 1Z1, Canada*
[3]*Mount Stromlo Observatory, The Australian National University, Weston Creek, ACT 2611, Australia*
[4]*Anglo-Australian Observatory, PO Box 296, Epping, NSW 2111, Australia*
[5]*Space Telescope European Coordinating Facility, European Southern Observatory, Karl-Schwarzschild Strasse 2, 85748, Garching, Germany*
[6]*Astrophysics Group, HH Wills Physics Laboratory, University of Bristol, Tyndall Avenue, Bristol BS8 1TL*

ABSTRACT

We present spatially resolved intermediate-resolution spectroscopy of a sample of 12 E+A galaxies in the $z = 0.32$ rich galaxy cluster AC 114, obtained with the FLAMES multi-integral field unit system on the Very Large Telescope (VLT) of the European Southern Observatory. Previous integrated spectroscopy of all these galaxies by Couch & Sharples had shown them to have strong Balmer line absorption and an absence of [O II]λ3727 emission – the defining characteristics of the 'E+A' spectral signature, indicative of an abrupt halt to a recent episode of quite vigorous star formation. We have used our spectral data to determine the radial variation in the strength of Hδ absorption in these galaxies and hence map out the distribution of this recently formed stellar population. Such information provides important clues as to what physical event might have been responsible for this quite dramatic change in star formation activity in the recent past of these galaxies. We find a diversity of behaviour amongst these galaxies in terms of the radial variation in Hδ absorption: four galaxies show little Hδ absorption across their entire extent; it would appear they were misidentified as E+A galaxies in the earlier integrated spectroscopic studies. The remainder show strong Hδ absorption, with a gradient that is either *negative* (Hδ equivalent width decreasing with radius), *flat* or *positive*. By comparison with numerical simulations we suggest that the first of these different types of radial behaviour provides evidence for a merger/interaction origin, whereas the latter two types of behaviour are more consistent with the truncation of star formation in normal disc galaxies with the Hδ gradient becoming increasingly positive with time after truncation. It would seem therefore that more than one physical mechanism is responsible for E+A formation in the same environment.

Key words: galaxies: clusters: individual: AC 114 – galaxies: evolution – galaxies: formation.

1 INTRODUCTION

'E+A' galaxies exhibit strong Balmer absorption lines superimposed upon an elliptical galaxy type spectrum (Dressler & Gunn 1983) and represent a population of galaxies that have undergone a significant change in their star formation rate. The lack of optical emission lines, for example [O II]λ3727, indicates that star formation has ceased. However, the strong Balmer absorption line signature implies the existence of a substantial population of young A stars which must have formed no more than $\sim$1 Gyr ago. This spectral

signature is usually interpreted as the recent truncation of a starburst (Dressler & Gunn 1983; Couch & Sharples 1987, hereafter CS87; Barger et al. 1996; Poggianti et al. 1999) or the abrupt truncation of more normal star formation activity in a disc galaxy (CS87; Balogh et al. 1999).

The numbers of E+A galaxies seen in different environments evolves strongly with redshift. E+A galaxies are rare in nearby clusters, making up only about 1 per cent of the total galaxy population in the clusters (Fabricant, McClintock & Bautz 1991), and are even less common in the low-redshift field, comprising roughly 0.03 per cent – 0.2 per cent of the overall galaxy population depending on the selection criteria (hereafter Z96; Blake et al. 2004). In contrast, these galaxies represent a significant fraction of the galaxy population in

★E-mail: mpracy@phys.unsw.edu.au

intermediate redshift clusters, where they were initially discovered by Dressler & Gunn (1983). Estimates of the fraction of E+A galaxies in such ($0.2 < z < 0.6$) clusters generally range from 10 to 20 per cent (Dressler & Gunn 1992; Couch et al. 1998; Dressler et al. 1999), although this high fraction may not be a universal property of all clusters at these redshifts (Balogh et al. 1999).

The physical processes involved in the formation of these galaxies remain unclear; however, it is unlikely that such a dramatic change in star formation activity could be owing to internal factors and hence external 'environmental' influences would seem to be the cause. In this regard, a plethora of possible mechanisms have been suggested including major mergers (Mihos & Hernquist 1996), minor mergers and galaxy–galaxy interactions or, in the case of E+A galaxies residing in clusters, interaction with the strongly varying cluster tidal field (Bekki 1999), galaxy harassment (Moore, Lake & Katz 1998) or interaction with the hot intracluster medium (Gunn & Gott 1972). There is mounting evidence that E+A galaxies in the low-redshift field are the result of mergers or tidal interactions. Z96 inspected ground-based imaging of a sample of 21 E+A galaxies drawn from the Las Campanas Redshift Survey (LCRS), and found a high incidence of tidal features in these galaxies implying mergers or galaxy–galaxy interactions in the formation process. This conclusion was later verified using high-resolution *Hubble Space Telescope* (*HST*) imaging (Yang et al. 2004). Blake et al. (2004) arrived at a similar conclusion using a larger sample drawn from the Two Degree Field Galaxy Redshift Survey (2dFGRS; Colless et al. 2001). Goto (2005) using a sample of 266 E+A galaxies from the Sloan Digital Sky Survey (Abazajian et al. 2004) claimed to observe an excess in the projected local galaxy density on scales of <100 kpc surrounding the E+A galaxies – indicating dynamical interactions as a likely formation mechanism.

Norton et al. (2001) obtained long slit spectroscopy of the Z96 sample in order to probe the spatial and kinematic distribution of the stellar populations. In most cases they found the young stellar population to be pressure supported, consistent with a merger origin. The study of 2dFGRS E+A galaxies by Blake et al. (2004) supported this picture by demonstrating that these galaxies are preferentially spheroidal systems, as evidenced by their morphologies, group environments and luminosity function.

In contrast to the field E+A galaxies the picture for E+A galaxies that reside in the dense cluster environment is less clear. The *HST* studies of Couch et al. (1994, 1998) and Dressler et al. (1999) revealed that the majority of E+A galaxies in intermediate redshift clusters are undisturbed elliptical or early-type disc systems. The very existence of such disc systems rules out equal mass mergers that would disrupt the disc (Dressler et al. 1999), although minor mergers with a gas-rich dwarf remains a plausible formation mechanism (Bekki, Shioya & Couch 2001). In the one example of spatially resolved spectroscopy of a high-redshift ($z \approx 0.18$) cluster E+A, Franx (1993) found evidence for strong rotation in the young stellar population.

Knowledge of how this population of recently formed stars in E+A galaxies is distributed *spatially* is critical information for differentiating between the proposed formation mechanisms. Mergers and tidal interactions lead to a centrally concentrated burst of star formation (Mihos & Hernquist 1996, Bekki et al., in preparation) with the starburst contained within the central 1–2 kpc. By contrast, ram pressure stripping should lead to a roughly uniform truncation of star formation across the disc (Rose et al. 2001). Using a combination of long slit spectroscopy and broadband imaging Rose et al. (2001) studied the spatial distribution of recent star formation in early-type galaxies in three low-redshift clusters and found that the

star formation was centralized in comparison to the distributions observed in similar galaxies in the field. Bartholomew et al. (2001) measured the colour gradients of early-type galaxies in a $z \approx 0.33$ cluster and found that the E+A galaxies tended to have bluer nuclei than the overall galaxy population, implying systematically more centralized star formation.

In this paper we present new data on the spatial distribution of Hδ absorption – one of the key tracers of the young stellar population – for a sizeable sample of E+A galaxies in a rich intermediate redshift cluster. In contrast to previous studies, ours is the first to obtain such information via integrated field unit (IFU) spectroscopy on an 8-m telescope (the Very Large Telescope, VLT). If mergers and tidal interactions are responsible for the E+A galaxy signature, then a strong *negative* radial gradient in Hδ equivalent width is expected, in the sense that the Hδ equivalent width decreases with galactocentric radius (Bekki et al., in preparation). However, if the E+A signature is the product of the truncation of normal star formation, a more uniform distribution of Hδ equivalent width across the galaxy is expected. Our target sample comprises 12 E+A galaxies that are members of the $z = 0.32$ rich cluster AC 114 (also known as Abell S1077; Abell, Corwin & Olowin 1989), which has been the subject of many previous studies as a result of its significant population of blue 'Butcher–Oemler' galaxies CS87. It has a high velocity dispersion $\sigma = 1660$ km s^{-1} (Mahdavi & Geller 2001) and an irregular X-ray morphology (De Filippis et al. 2004).

The layout of this paper is as follows: in Section 2 we provide all the details relevant to the observational data used in our study, describing how our E+A sample was selected, giving details of our IFU spectroscopic observations, outlining how the data were reduced, and discussing difficulties encountered with the position of the IFUs on our target galaxies. In Section 3 we first examine our spectra in their integrated form (i.e. summed over the entire galaxy), comparing them with the original integrated spectroscopy obtained by CS87 and thus verifying these galaxies' classification as E+A types based on this previous lower resolution and signal-to-noise spectral data. In Section 4 we then exploit the spatially resolved nature of our spectroscopy to map out the location of the young stars within our E+A galaxies, using the equivalent width of the Hδ absorption line, as defined by the H$\delta_{\rm F}$ index (Worthey & Ottaviani 1997), as our tracer. In particular, we determine how H$\delta_{\rm F}$ varies with radius across each galaxy, taking into account the convolving effects of astronomical seeing. We discuss and interpret our results in Section 5, using model predictions for the radial gradients in metallicity and Hδ strength under different formation scenarios as our main tool. Our main conclusions are summarized in Section 6. Throughout this paper we adopt an $\Omega_{\rm M} = 0.3$, $\Omega_\Lambda = 0.7$ and $H_0 = 70$ km s^{-1} Mpc^{-1} cosmology, which places AC 114 at a comoving distance of 1231 Mpc, with 1 arcsec projecting to 4.6 kpc.

2 DATA

2.1 Sample selection

We targeted the members of AC 114 which had been previously identified as E+A galaxies in the spectroscopic study of this cluster conducted by CS87. We chose the brightest ($R \leqslant 20.3$) galaxies from the CS87 sample, and paid no attention to their colour in our selection. This meant we included both the reddest E+A galaxies – which CS87 referred to as 'red Hδ-strong' (HDS) galaxies and have enhanced Balmer line absorption even though their colours are as red as passive E/S0 galaxies – as well as those with bluer colours – which CS87 referred to as 'post-starburst' (PSG) galaxies, because they are

Table 1. Summary of the photometric, spectroscopic and morphological properties of our sample (see text for details).

CN No.	R	Hubble type	Spec class	$b_J - r_F$	Hδ CS87
143	20.31	Sbc	PSG	1.67	7.7
187	19.31	S0	HDS	2.29	3.4
191	19.69	Sa	PSG	1.61	5.6
228	19.90	Sab	PSG	1.38	5.1
22	19.73	pec	PSG	1.47	8.1
247	19.12	E	HDS	2.44	2.8
254	20.09	S0/a	PSG	1.99	6.5
4	18.44	E	HDS	2.29	4.7
667	19.37	Sb	?	1.67	?
849	19.71	Sab	PSG	1.82	4.6
858	19.12	E	HDS	2.35	3.8
89	19.61	E	HDS	2.23	5.6

presumably seen much sooner after the cessation of star formation. All of these galaxies have no detectable [O II]$\lambda3727$ emission. Also included in our sample was the blue galaxy CN 667, for which the CS87 study was able to confirm its membership of AC 114 but not its spectral type. This gave us a sample of 12 galaxies.

In Table 1 we list the photometric, spectroscopic and morphological properties of this sample: column (1) gives the identity number of the galaxy from the original Couch & Newell (1984) catalogue, column (2) gives the R-band magnitude, column (3) gives the *HST*-based Hubble types determined by Couch et al. (1994, 1998), column (4) gives the PSG/HDS spectral subtype assigned by CS87, column (5) gives the $b_J - r_F$ colours, and column (6) gives the rest-frame Hδ equivalent width values (Å) measured by CS87. Postage stamp images of all the galaxies taken in the F702W passband with *HST*, are displayed in Fig. 1. As can be seen, the galaxies generally have an early-type (E, S0, Sa–b) morphology, the exception

being CN 22 which has a peculiar morphology and was classified by Couch et al. (1998) as an advanced merger.

2.2 Spectroscopic observations

We obtained intermediate-resolution IFU spectroscopy of our sample with the VLT–Kueyen telescope. We used the Fibre Large Array Multi-Element Spectrograph (FLAMES) system in the mode where it couples the OzPos multi-object fibre positioner to the GIRAFFE spectrograph. OzPos is able to deploy 130 single 'Medusa' fibres or 15 individual IFUs over a 25-arcmin field at the Nasmyth focus of the telescope. We utilized the latter to observe the 12 galaxies in our sample simultaneously; the remaining three IFUs were used to observe blank sky regions in order to facilitate accurate sky subtraction. Each IFU has a 3×2 arcsec^2 (13.8×9.2 kpc^2) field of view which is sampled spatially by 20 square 0.5-arcsec lenslets; its geometry is shown in Fig. 2.

The observations were obtained during the nights of 2003 September 23, 26 and 27, being taken when the seeing conditions were at their best. A total of 17 exposures, mostly of 1800-s duration, were obtained over these three nights, in seeing which ranged from 0.54 to 0.84 arcsec. They gave a combined exposure time of 29 119 s, during which the time-weighted mean seeing was 0.75 arcsec (corresponding to a physical scale of 3.5 kpc at the redshift of the cluster). The GIRAFFE spectrograph was used in its 'low-resolution' $R = 6000$ mode and in the 'LR4' wavelength setting. This configuration allowed us to observe over the wavelength interval $5015 \leqslant \lambda \leqslant 5831$ Å($3780 \leqslant \lambda_{rest} \leqslant 4420$ Å at $z = 0.32$) at a dispersion of ~ 0.2 Å pixel^{-1}.

2.3 Data reduction

The data were reduced using standard IRAF routines. In brief, each frame was first bias subtracted and then its overscan region removed.
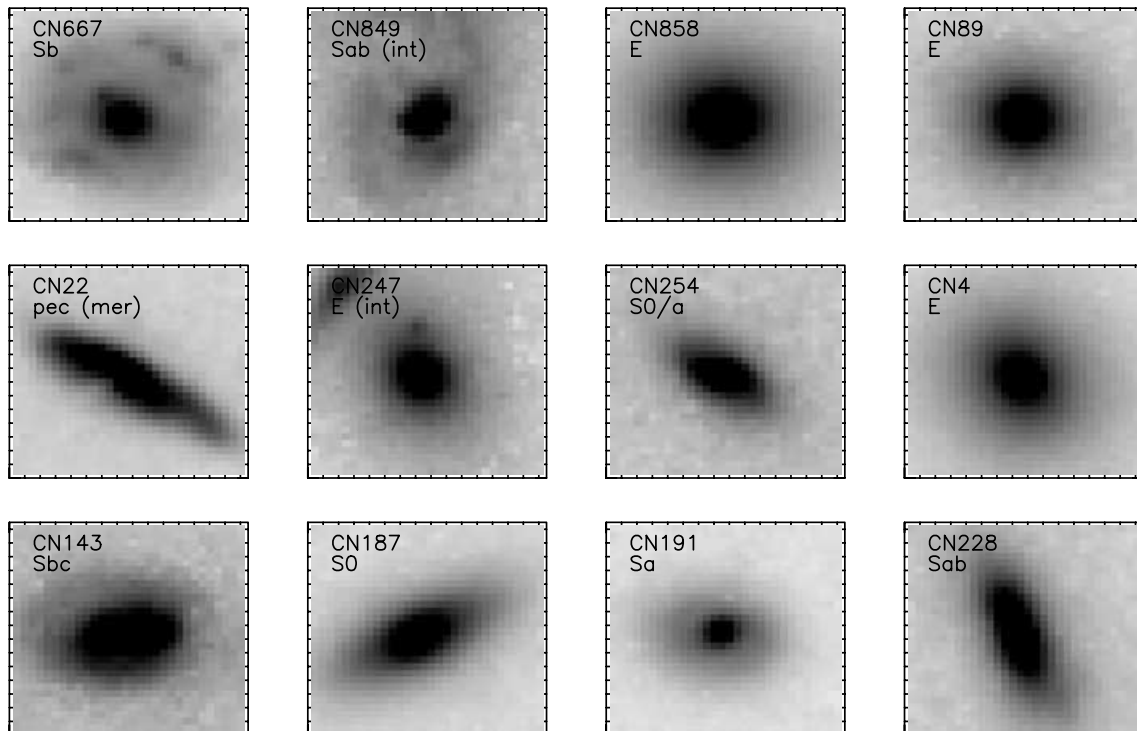
Figure 1. *HST* Wide Field Planetary Camera 2 (WFPC2) images of the E+A galaxy sample. Each image has dimensions 3×3 arcsec^2, corresponding to approximately 13.8 kpc at the cluster redshift and comparable to the total IFU aperture.
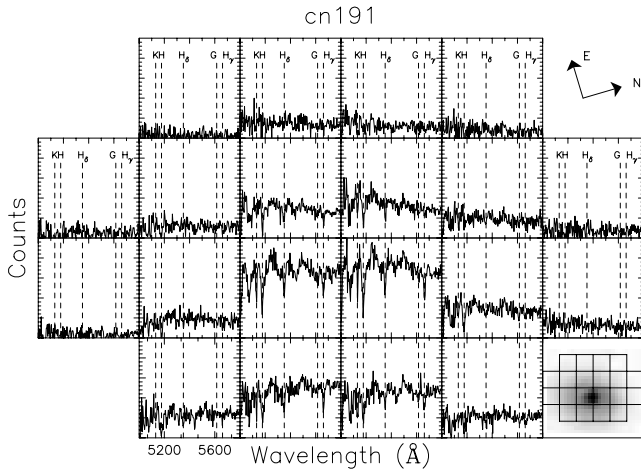
Figure 2. Spatial geometry of the IFUs used in our study. Each square represents an IFU lenslet, which is 0.5 arcsec on a side. The spectrum obtained through that lenslet (for CN 191) is displayed within. The ordinate scale is identical in all lenslets; thus the continuum level reflects the level of light observed in that direction on the sky. Note the astrometric offset, which is discussed in Section 2.4. The bottom right panel shows the *HST* image of CN 191 and its orientation with respect to the IFU.
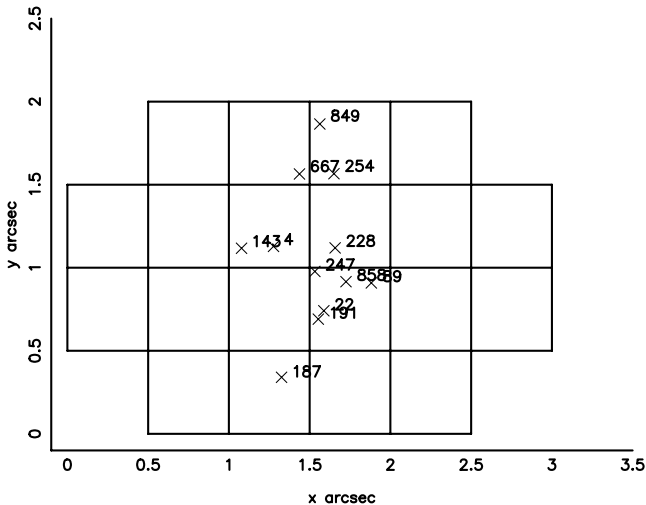
Figure 3. The centroid positions of our galaxies within the IFU field; objects are labelled with their CN number.

All science frames from a given night were then median combined, after having been scaled to allow for the different exposure times. Cosmic ray rejection was performed as part of this process using the CRREJECT algorithm. The flat-fields were used to identify the position of the spectra on the CCD. A smoothed scattered light signal was removed from the flat-field and science frames by fitting a Chebyshev function to the pixels between the fibres. Following this, the spectra were extracted and wavelength calibrated using arc lamp exposures. The flat-field spectra were used to calculate and correct for the variations in throughput from fibre to fibre; this was based on the total signal contained within each spectrum over the entire wavelength interval covered by our observations. Finally, all the spectra recorded through the three 'blank sky' IFUs were summed and averaged to form a mean 'sky' spectrum, which was then used to subtract the sky from the spectra recorded in the remaining 12

'target' IFUs. The spectra were corrected to a relative flux scale using an ARGUS–IFU observation of a flux standard star.

Systematic errors in the sky subtraction will lead to incorrect continuum levels in the spectra and hence to biased equivalent width measurements. In order to evaluate the accuracy of the sky subtraction we used the residuals of the individual 'sky' spectra after subtraction of the 'mean sky' signal. Using the residual in the $\lambda 5577$ atmospheric emission line we calculated the fractional error in the sky subtraction to be 3.6 per cent, this compares with 1.1 per cent expected from Poisson statistics. More importantly, we checked for any systematic errors in the sky subtraction using the residual continuum. We calculated the rms of the mean value of the residuals in each lenslet and the mean rms of the residuals averaged over all lenslets, the ratio of these gives the size of any systematic errors in the sky subtraction with respect to the size of purely random errors. The resulting ratio is 0.14 implying that any systematic sky-subtraction error is roughly an order of magnitude smaller than the random errors.

2.4 IFU–object placement

At this point of having derived accurately sky-subtracted spectra for the 20 lenslets in each IFU, it became apparent that most of our target galaxies were not perfectly centred in each IFU. An example is shown in Fig. 2 where we plot the spectra obtained in each of the IFU 'pixels' for the galaxy CN 191. Note that the normalization of each spectrum is identical, so the continuum level of the 20 spectra can be directly compared. We see quite clearly in this case that the signal is at a maximum in the two spectra immediately below the centre of the IFU, indicating that the galaxy is off-centre in this direction by ~0.25–0.50 arcsec.

In Fig. 3 we display the centroid positions of each galaxy within the IFU field, estimated from the total galaxy signal observed in each IFU pixel (see Section 4.2). The centroid positions of each galaxy in the coordinate system of Fig. 3 are listed in columns (5) and (6) of Table 2. It can be seen from Fig. 3 that the galaxies are generally off-centre by at least half an IFU pixel 0.25 arcsec, with quite a number being off-centre by as much as 1–2 IFU pixels 0.5–1.0 arcsec. This could be owing to one or more of the following factors: (i) errors in the astrometric positions used for our galaxies; (ii) IFU positioning errors; and (iii) errors in the determination of the galaxy centroids from our IFU data.

As the placement of the IFUs on target objects involves bringing them in approximately radially from their parked locations around the perimeter of the field, the IFUs will generally all be at different position angles with respect to the sky. Hence Fig. 3 gives no sense as to whether the three possible sources of error above are random or systematic. In Fig. 4, therefore, we plot the observed positional offsets in terms of their magnitude and direction on the sky. The vectors point in the direction of the calculated centre of the galaxy from the geometric centre of the IFU, and their lengths have been scaled up by a factor of 100 for display purposes. It would appear from this diagram that the positional errors are systematic on the sky, with perhaps marginal evidence that their magnitude increases with distance from the centre of the field. This implies there is some systematic problem with the IFU positioning across the field, either with the OzPos positioner or, more likely, in there being a systematic positional offset between the astrometric zero points for our guide stars (which are not plotted in Fig. 4) and that of our target galaxies. As disappointing as it may be, we are left to conclude that this problem is most likely owing to a combination of all three of the different types of error mentioned above, although we note that

Table 2. Columns from left to right: galaxy ID, redshift, observed $b_J - r_F$ colour, K correction, galaxy centres in the $x - y$ reference frame defined in Fig. 3, effective radius measured from the *HST* images, Hδ equivalent width from CS87, Hδ_F from spatially integrated FLAMES spectra, Hγ_F from spatially integrated FLAMES spectra, slope of the Hδ_F radial profiles (normalized to the effective radius) and the radial profile slopes corrected for the effects of astronomical seeing.[a]

CN No.	z	$b_J - r_F$	$K_{b_J - r_F}$	x_{cen} (arcsec)	y_{cen} (arcsec)	r_e (kpc)	Hδ CS87 (Å)	Hδ_F (Å)	Hγ_F (Å)	Slope (Hδ_F) ($\text{Å}\, r_e^{-1}$)	Corr. slope ($\text{Å}\, r_e^{-1}$)
143	0.310	1.67	0.64	1.08	1.12	3.2	7.7	4.18 ± 0.59	4.36 ± 0.48	0.80 ± 1.68	1.6
187	0.307	2.29	1.03	1.33	0.34	2.6	3.4	-0.62 ± 0.56	-2.39 ± 0.42	-0.69 ± 0.67	-1.8
191	0.305	1.61	0.60	1.55	0.69	1.9	5.6	3.20 ± 0.38	3.90 ± 0.31	-2.37 ± 0.44	-6.4
228	0.316	1.38	0.46	1.66	1.12	3.4	5.1	5.82 ± 0.66	5.67 ± 0.56	1.96 ± 0.85	5.8
22	0.336	1.47	0.53	1.59	0.74	3.4	8.1	4.50 ± 0.38	NA	-2.47 ± 0.80	-5.8
247	0.319	2.44	1.15	1.53	0.98	1.9	2.8	1.65 ± 0.56	-0.41 ± 0.41	-0.14 ± 0.55	-0.2
254	0.319	1.99	0.86	1.65	1.57	2.7	6.5	2.24 ± 1.22	2.10 ± 1.00	-1.48 ± 1.45	-4.3
4	0.308	2.29	1.04	1.28	1.13	5.2	4.7	-1.03 ± 0.38	-1.13 ± 0.28	1.30 ± 1.60	2.6
667	0.312	1.67	0.64	1.44	1.56	4.4	?	0.11 ± 0.50	0.99 ± 0.38	0.77 ± 1.32	1.3
849	0.324	1.82	0.75	1.56	1.87	2.6	4.6	3.64 ± 0.30	0.75 ± 0.24	0.84 ± 0.40	2.1
858	0.312	2.35	1.00	1.73	0.92	3.8	3.8	-0.77 ± 1.15	-1.51 ± 0.88	2.17 ± 2.03	6.1
89	0.317	2.23	1.01	1.88	0.91	2.8	5.6	2.60 ± 0.65	-0.77 ± 0.57	0.39 ± 0.89	0.9

[a]Note the redshift of CN 22 precludes the measurement of the Hγ_F index.
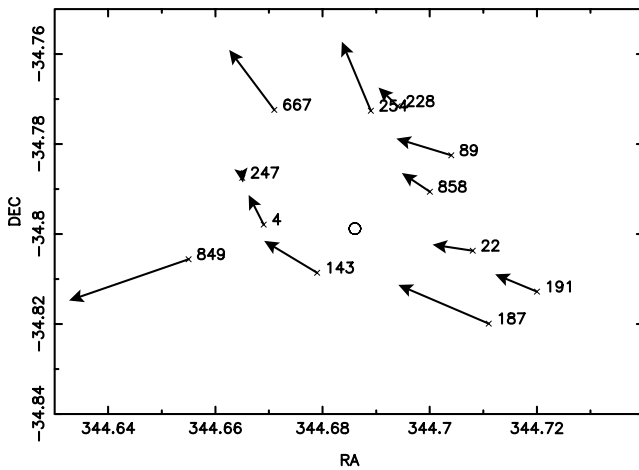
Figure 4. Vectors showing the magnitude and direction of the positional offsets of our target galaxies within the IFUs, as they appear on the sky. The lengths of the vectors have been scaled by a factor of 100 for display purposes. The circle indicates the centre of the FLAMES field of view.

repeated tests of the OzPos positioner have indicated it is capable of placing the IFUs to a rms precision of better than 0.2 arcsec. How we deal with this problem in our subsequent analysis is further detailed in Section 4.2.

3 SPATIALLY INTEGRATED SPECTRA

3.1 Construction and measurement

Before utilizing the spatially resolved spectroscopic information provided by our observations, it is instructive to first examine it in its 'integrated' form and see how our spectra compare with those previously obtained by CS87. For each galaxy, we combined the 20 individual spectra obtained with each IFU into a single spatially integrated spectrum. Each spectrum was weighted according to its variance to maximize the signal-to-noise ratio of the final integrated spectrum. The spectra for the 12 galaxies are presented in Fig. 5, having been smoothed with a Gaussian of FWHM 1.2 Å. It can be seen that these integrated spectra are of reasonably high quality

with the signal-to-noise (S/N) ratio ranging from $\sim$5 [Å^{-1}] for CN 254 to $\sim$20 [Å^{-1}] for CN 849, measured in a 100-Å wide interval (rest frame) just redwards of the Hδ feature. Their signal-to-noise ratios are certainly higher than those of the original spectra obtained by CS87. As such, the key spectral lines within our observed wavelength range (indicated by the vertical dashed lines in Fig. 5) are easily identifiable, in particular the Balmer absorption lines Hδ and Hγ. However, these two Balmer lines are conspicuous by their weakness or even absence in several of the galaxies (CN 858, 667, 4, 187), bringing into question their classification as E+A types.

These visual impressions were properly quantified by conducting redshift and spectral line index measurements. Redshifts were measured for each spectrum using the IRAF task FXCOR, which performs a Fourier cross-correlation (Tonry & Davis 1979) of the object spectrum with a set of template spectra taken from Vazdekis (1999). The resulting redshifts for our 12 target galaxies are given in column (2) of Table 2. These redshifts are in good agreement with those originally derived by CS87 with the rms difference between the two sets of redshifts being $\Delta z_{rms} \approx 0.001$.

These redshifts were then used to precisely locate spectral lines within each spectrum and measure their equivalent width. Of primary importance here is the Hδ line, given its use in defining an E+A galaxy (CS87; Dressler et al. 1999). To measure the equivalent width of this line we adopted the Hδ_F index definition of Worthey & Ottaviani (1997), whereby the signal within the line is evaluated over the rest-wavelength interval 4091.00–4112.25 Å, and the neighbouring continuum levels are determined within the intervals 4057.25–4088.50 and 4114.75–4137.25 Å. The error in this index was calculated directly from the variance array of the spectrum (see Cardiel et al. 1998). The Hδ_F values derived in this way are plotted in Fig. 6 (filled circles) and listed in column (9) of Table 2, for comparison the Hγ_F index values are given in column (10) of Table 2 and generally scale well with Hδ_F.

3.2 Comparison with CS87

It is worthwhile comparing our line index measurements with those of CS87, and re-examining their E+A status. In Fig. 6 we plot the Hδ equivalent width values of CS87 against our own. The first comparison we make is with our Hδ_F index values; this is shown
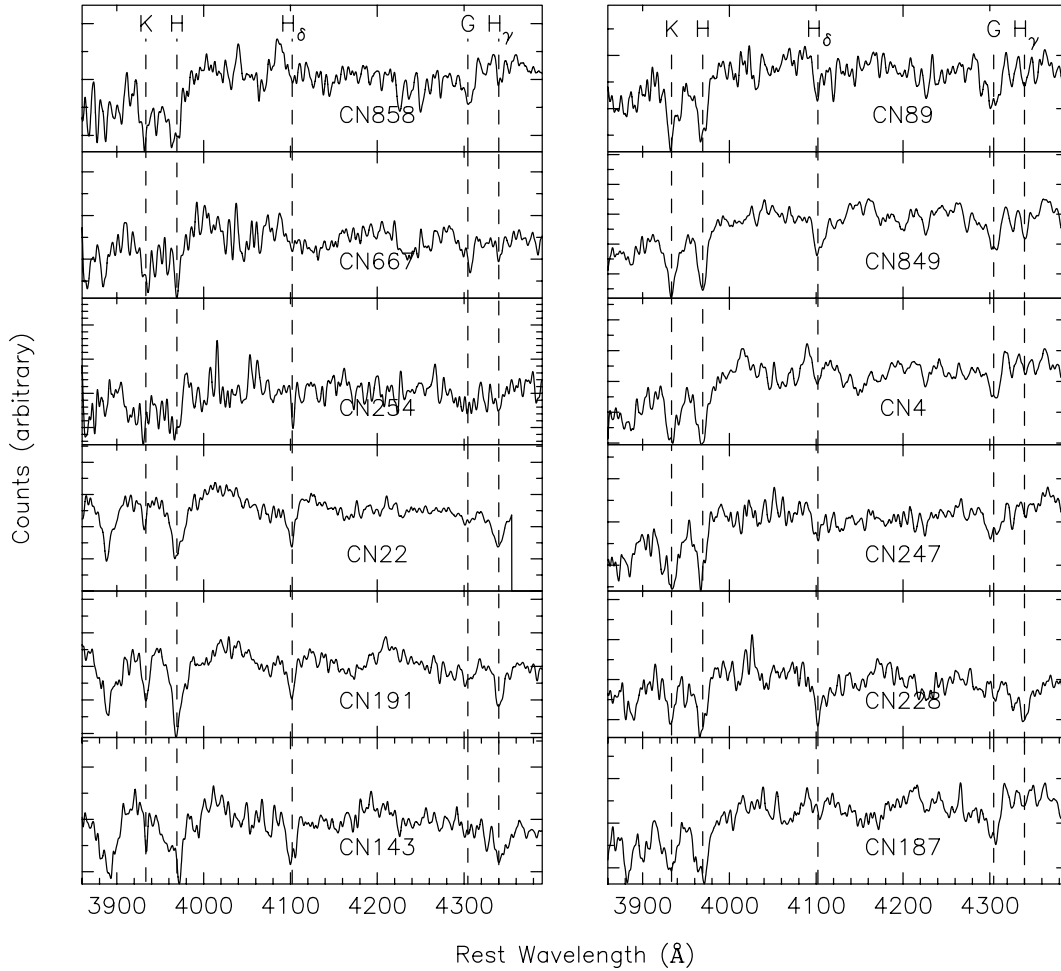
Figure 5. Spatially binned redshift-corrected spectra for the 12 galaxies in our E+A galaxy sample.
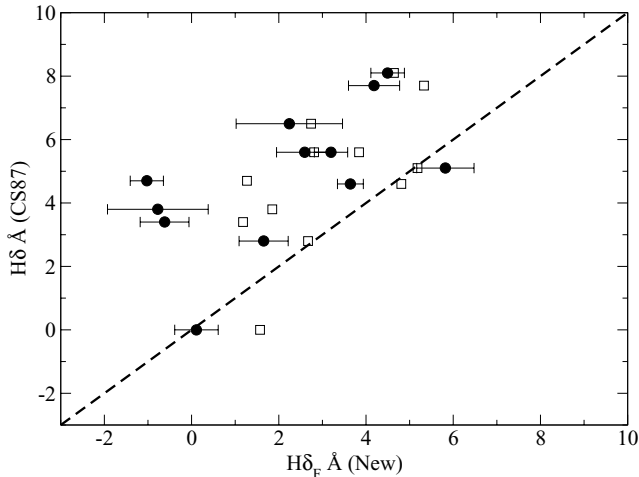
Figure 6. The $H\delta$ equivalent width values from CS87 versus those measured from our spatially integrated spectra (shown in Fig. 5). The filled circles show the comparison with our $H\delta_F$ index values; the open squares show the comparison with the values we obtain using the same interactive equivalent width measuring technique as that used by CS87. The point with a CS87 $H\delta$ value of zero corresponds to CN 667 for which no equivalent width measurement was made.

by the filled circles. A low value of $H\delta_F$ ($H\delta_F \approx 0$) is detected in galaxies CN 858, 667, 4 and 187, confirming the visual impressions mentioned above. As noted earlier, the spectral classification of CN 667 was previously uncertain CS87, and we can now confirm it to be 'passive' or, in the nomenclature of Dressler et al. (1999), a 'k' type. Note because no CS87 $H\delta$ equivalent width index is available for CN 667, it is arbitrarily assigned an ordinate value of zero in Fig. 6. The other three galaxies were, however, all classified as E+A galaxies; our better quality and higher spectral resolution data clearly show these classifications to be incorrect. It can be seen, in Fig. 6, that our measured $H\delta_F$ indices are generally smaller than the CS87 values, the average difference being ~ 2.7 Å. However, we caution that CS87 used a different method for measuring the equivalent widths of lines in their spectra, and their integrated spectra were measured through a 2-arcsec aperture fibre, the exact positioning of which on each galaxy cannot be determined.

While we are unable to determine what, if any, aperture effect the latter might introduce into our comparison, we can at least address the issue of different line measuring techniques. To do so, we re-measured the $H\delta$ equivalent width values of our spatially integrated spectra using the same 'interactive' routine that CS87 used (the routine ABLINE in the FIGARO package). Here, the line and neighbouring continuum regions are identified interactively, an iterative polynomial fit is performed to determine the continuum level across the line, and the line itself is fitted by a Gaussian

function within the wavelength interval identified. As spectral resolution can affect the measured equivalent width values, we were careful to first smooth our spectra to the resolution of the original CS87 spectroscopy. The comparison with the Hδ equivalent width values measured using this technique is shown in Fig. 6 by the open squares. It can be seen that while our measurements are still systematically smaller than those of CS87, the difference is nowhere near as great (cf. the Hδ_F measurements), the mean difference being ~ 1.7 Å. Nonetheless, our comparison points to the fact that systematic differences in line index measurements can exist between different studies and data sets, and some caution needs to be exercised accordingly. One obvious cause of such differences, particularly for multi-object fibre-based studies, is a systematic error in sky subtraction. This would lead to incorrect continuum levels within the spectra, and hence an over- or underestimation of the equivalent widths.

Hereafter, we only consider the eight galaxies in our sample where we have detected significant (H$\delta_F > 1$ Å) Balmer absorption.

3.3 Spectrophotometric models revisited

With there having been some revisions to the measured strengths of the key Balmer absorption lines within our E+A sample, a re-examination of their evolutionary status is warranted. This is best done using the Hδ_F–colour diagnostic diagram CS87, where we compare the data for our galaxies with spectrophotometric models. This is shown in the top panel of Fig. 7, where we plot the Hδ_F values measured for our galaxies against their $b_J - r_F$ colours (the reddening-corrected values taken from CS87). The spectra were smoothed to a resolution of 3 Å prior to measuring the Hδ_F indices in order to facilitate a consistent comparison with model spectra. We have K corrected the colours using the formulae given by Wild et al. (2004), which calculate a K correction based on redshift and colour

$$K_b = [-1.63 + 4.53x]y + [-4.03 - 2.01x]y^2 - \frac{z}{1 + (10z)^4}, \quad (1)$$

$$K_r = [-0.08 + 1.45x]y + [-2.88 - 0.48x]y^2, \quad (2)$$

where $x = b_J - r_F$ and $y = z/(1 + z)$. The magnitude of the K correction for each galaxy is given in column (4) of Table 2.

Also plotted in the top panel of Fig. 7 are the evolutionary tracks for galaxies with different star formation histories; these were calculated using the stellar population synthesis models of Bruzual & Charlot (2003). The Bruzual and Charlot code returns line index measurements and $B - R$ colours at a series of time steps for the chosen star formation history computed directly from synthetic model spectra at 3-Å resolution. It is important to note that the line index measurements here were made using the same Hδ_F definition (at the same spectral resolution) that was applied to our observed spectra, thereby ensuring complete consistency in comparing our observations with the models. As far as the model colours were concerned, they were transformed into $b_J - r_F$ values using the conversion of Couch (1981)

$$b_J - r_F = -0.017 + 1.059 (B - R) - 0.027 (B - R)^2. \quad (3)$$

In all cases we assumed a Salpeter (Salpeter 1955) initial mass function and an exponentially decaying star formation rate. The solid curves in the top panel of Fig. 7 trace the evolution in the Hδ-colour plane for solar metallicity models in which this exponentially decaying star formation is abruptly (instantaneously) truncated after
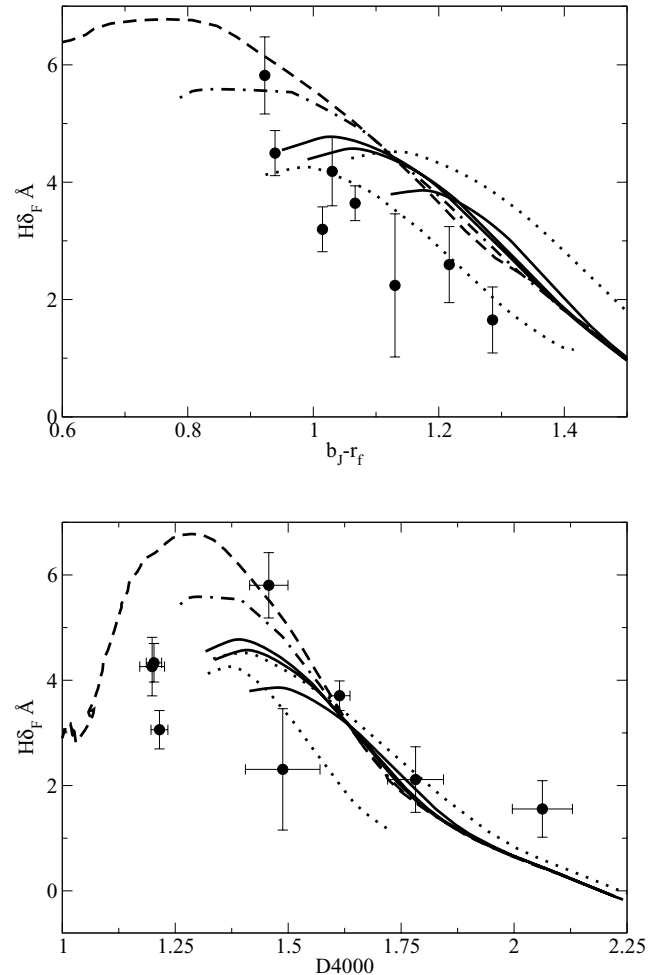
Figure 7. Top panel: Hδ_F plotted against $b_J - r_F$ colour. The Hδ_F measurements from our sample are plotted as filled circles. The galaxy colours have been corrected for reddening CS87 and K correction. The curves are evolutionary tracks produced using the spectral synthesis models of Bruzual & Charlot (2003). The solid lines represent evolutionary tracks for models in which normal star formation is suddenly truncated. The dashed and dot-dashed lines show the evolution for a PSG. The dotted lines show the effect of varying metallicity. The details of these models are described in the text. Bottom panel: Hδ_F plotted against the D4000 index. The model curves are the same as those shown in the top panel.

10 Gyr. The model curves are shown from the time the star formation is truncated to a time 10 Gyr after the end of star formation. The models displayed have exponentially decaying star formation rates with e-folding times $\tau = 5$, 10 and 15 Gyr. The $\tau = 15$-Gyr model has the highest value of Hδ_F and bluest colour at the time the star formation is truncated (because it has the highest star formation rate at this time). The $\tau = 5$ and 10-Gyr models have progressively lower Hδ_F index values and redder colours. The dashed curve represents a $\tau = 5$ Gyr model in which a δ-function burst of star formation occurs after 10 Gyr, converting 10 per cent of the total galaxy mass into new stars. The dot-dashed curve is a variation of the starburst model in which the starburst, converting 10 per cent of the galaxy mass into stars, takes place over a period of 1 Gyr. In order to investigate the effect of metallicity on these evolutionary tracks in the Hδ_F–colour plane, we also plot the tracks of the $\tau = 10$ Gyr model for subsolar (Fe/H $= -0.64$) and supersolar (Fe/H $= 0.56$) metallicities. These are shown as the dotted lines in the top panel of Fig. 7.

The lower metallicity model track is shifted to have bluer colours than in the case of solar metallicity and the high-metallicity track is shifted redward. Note the almost monotonic increase of observed $H\delta_F$ with increasing blueness. This is consistent with the general trends seen in all the model tracks. However, apart from the low-metallicity models, the data points in the top panel of Fig. 7 all lie blueward and/or beneath the model curves. This may be a result of errors in, any or all of, the reddening correction, colour conversion and K correction causing the data to have colours which are too blue. Emission-line filling from residual star formation present in the data but not in the models resulting in lower values of the measured $H\delta_F$ index could also explain the discrepancy. In the bottom panel of Fig. 7 we show the galaxies in the $H\delta_F$–D4000 plane. We use the D4000 index definition of Balogh et al. (1999) which measures the ratio of the flux in a band just redward of the 4000 Å break (4050–4150 Å) to the flux in a band just blueward of the 4000-Å break (3850–3950 Å). This index is less affected by dust than broadband colours and does not rely on uncertain colour conversions and K corrections. The same set of models described above are superimposed on the data and, in this case, there is no systematic offset in the D4000 index value between the model tracks and observational data.

It is apparent from the tracks in Fig. 7 that it is difficult to distinguish between the truncation of a starburst episode and the abrupt truncation of normal star formation, unless the galaxy is observed shortly after the starburst when it will display bluer colours and stronger Balmer line absorption than can be reproduced by the truncation of normal star formation (upper left region of Fig. 7). *We are unable to differentiate between the truncation of exponentially decaying star formation and the sudden cessation of a starburst, on the basis of the 'integrated' $H\delta$ equivalent widths and broadband colours alone.* It is worth noting that the duration over which these models can be distinguished is very short. For the starburst models presented in Fig. 7, the interval between the time star formation ceases and the model galaxy evolves redwards of $b_J - r_F > 1.0$, is approximately 600 Myr. The short lifetime of this very blue HDS phase implies that very few galaxies should be observed in this part of parameter space.

4 SPATIALLY RESOLVED SPECTRA

4.1 Defining the galaxy centre

Owing to our target galaxies being off-centre within the IFUs (see Section 2.4), our first step prior to analysing our spatially revolved spectral data was to find where each galaxy was centred within the IFU. This was done by summing the flux in each IFU element over the full wavelength range of the spectra to create an image in the IFU of each galaxy. It is insufficient to simply calculate a flux-weighted mean position for the centre of the galaxy, because the small spatial extent of the IFU will cause us to underestimate the offset of the galaxy centre from the centre of the IFU. Instead we fitted a surface $z(x, y)$ to the IFU image

$$z(x, y) = a + bx + cx^2 + dy + ey^2 \qquad (4)$$

and required the coefficients c and e to both be negative. The galaxy centre is then defined by the maximum of the function $z(x, y)$

$$x_{cen} = \frac{-b}{2c} \quad \text{and} \quad y_{cen} = \frac{-d}{2e}. \qquad (5)$$

Our choice of function is motivated only by the requirement that it has a well-defined maximum; the precise choice of functional form

has little effect on the derived position of the maximum. In Fig. 3 we show the positions of the centre of the galaxies as determined from the maxima of the fitted paraboloids.

4.2 Radial profiles

The signal-to-noise ratio of the spectra obtained in each individual IFU lenslet is insufficient to accurately map the spectral line features at an individual IFU pixel scale (0 arcsec 5). Hence we spatially binned the IFU spectra in annuli around the galaxy centres, focusing our attention on *radial* variations in the spectral properties.

In binning the data in this way, the weight assigned to the ith lenslet was taken to be

$$w_i = \frac{f_i A_i}{\sum f_i A_i}, \qquad (6)$$

where f_i is the total flux observed through the lenslet, and A_i is the area of the lenslet which falls within the annular bin (the value for which was calculated numerically). The spectra were binned into three concentric annuli, which were partitioned at 0.5 and 1 arcsec. The outermost annulus contained all of the IFU spectra at radii greater than 1 arcsec, and its effective radius was taken as the midpoint between the 1-arcsec ring and the smallest ring which contained the entire IFU field of view. This results in a $\frac{S}{N}$ of $\sim$2–3$[\text{Å}^{-1}]$ for the outer bins of the faintest galaxies to a $\frac{S}{N}$ of $\sim$16$[\text{Å}^{-1}]$ for the central bin of CN 849. The $H\delta$ equivalent width measurements were then repeated on the binned spectra obtained in each of the three annuli.

The radial variation in $H\delta_F$ observed in each of our galaxies can be seen in Fig. 8, where we plot the values measured in the three annular bins. Radial gradients are seen in most galaxies, and for the purposes of our subsequent analysis (in particular, deconvolution; see below) we represent these via a linear fit to the data points

$$H\delta_F(r) = \alpha + \beta \frac{r}{r_e}, \qquad (7)$$

where r_e is the effective radius of the galaxies measured from the *HST* imaging and are given in column (7) of Table 2 and the slopes, β, being listed in column (11) of Table 2.
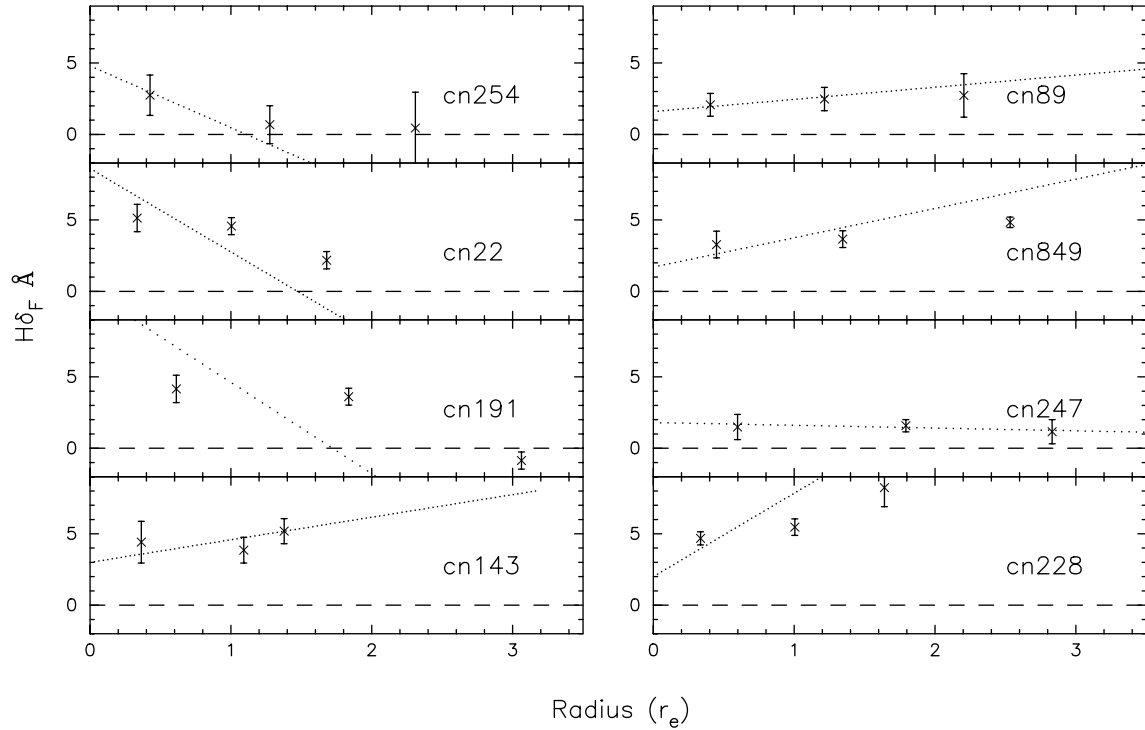
4.3 Deconvolving the seeing disc

The galaxy flux distributions that we observe across the IFU lenslets are convolved with a seeing disc which has a time-averaged FWHM (0.75 arcsec) which exceeds the side length of a lenslet (0.5 arcsec). We therefore expect the 'true' deconvolved radial equivalent width profile to differ significantly from that which is observed. Qualitatively, any observed equivalent width gradient will be more pronounced before convolution. In detail, we denote EW_{con} and F_{con} as, respectively, the equivalent width and flux maps after convolution with the seeing disc. Let EW_{dec} and F_{dec} be the deconvolved maps of these quantities. The equations governing the convolution (which is denoted by the overline symbol) are

$$F_{con} = \overline{F_{dec}},$$
$$F_{con} \times EW_{con} = \overline{F_{dec} \times EW_{dec}}. \qquad (8)$$

In light of the inherent difficulties in performing numerical deconvolutions of general functions, we adopted the following method to determine the 'true' equivalent width profile EW_{dec}, which we assume is a linear function of radius $EW_{dec}(r) = \alpha' + \beta'(r/r_e)$. First, we fitted an elliptical Gaussian to the pixelized map of F_{con}, and deconvolved this function analytically using the observed seeing FWHM to obtain F_{dec}. We then looped over a grid (α', β') of

Figure 8. Radial Hδ_F profiles for the eight strong Balmer absorption line galaxies in our sample. The stars represent the measured Hδ_F values and the dotted lines represent the radial gradients after deconvolution with the seeing disc. The radial distances are shown in units of the effective radii of the galaxies as measured from the *HST* images (Fig. 1).

profiles for EW$_{dec}$. For each grid point we deduced the resultant convolved map EW$_{con} = \overline{(F_{dec} \times EW_{dec})}/F_{con}$, which we binned radially for comparison with the linear fits to the observed [Hδ_F, r] data points (Table 2). The best-fitting values of (α', β') form our best model for the deconvolved radial equivalent width profile of each galaxy.

The revised slopes β' are listed for each galaxy in the final column of Table 2. We note that the corrections involved are substantial (a modification of the slope by a factor $\approx$2), and always serve to increase the significance of the slope detection. This can be seen visually in Fig. 8 where we have plotted dotted lines the 'deconvolved' linear relations; it is important to stress here that their behaviour is not simply determined by the radial variation seen in the observed Hδ_F values, but also the radial flux distribution of the galaxy!

5 DISCUSSION

5.1 General trends

Inspection of Fig. 8 (or Table 2), whether it be the observed data points or the more accentuated 'deconvolved' linear profiles, indicates three distinct types of behaviour in terms of the variation of Hδ_F with galactocentric radius as follows. (i) A *negative* slope, with Hδ absorption being strongest at the centre of the galaxy and decreasing roughly monotonically with increasing radius – the E+A galaxies in our sample which show this type of behaviour are CN 254, 22 and 191. (ii) A *flat* slope, with Hδ_F being uniform across the entire face of the galaxy – three galaxies show this type of behaviour, and they are CN 143, 89 and 247 (although arguably this latter galaxy is not an E+A type, owing to its Hδ absorption being too weak [H$\delta_F < 2$ Å]). (iii) A *positive* slope, with Hδ absorption be-

ing at its weakest at the centre of the galaxy and increasing roughly monotonically with increasing radius – the galaxies in this category are CN 849 and 228.

Curiously, however, there appears to be little correlation between Hδ profile slope and overall morphology. Two of the three negative-slope galaxies are early-type disc galaxies (CN 254, S0a; CN 191, Sa), and the two positive-slope galaxies have this morphology as well (CN 849 and 228 – both Sabs). The other negative-slope galaxy, CN 22, has a peculiar morphology and is clearly a merging system (which at least is consistent with its negative Hδ slope; see below). Two of the three flat-sloped galaxies, CN 89 and 247, are both ellipticals. The only other flat-sloped galaxy, CN 143, has an Sbc morphology, which we note is the latest Hubble type in our E+A sample. Finally, it should also be noted that merger/interaction activity appears to be prevalent amongst the positive and flat-sloped galaxies, with the *HST*-based imaging of Couch et al. (1998) providing quite clear evidence that CN 849 is interacting with its close, bright neighbour (with the two being connected by a tidal bridge), and somewhat more tentative evidence that CN 247 is involved in a similar interaction with its neighbour. Although CN 849 is an interacting galaxy (it is clearly not in the late stage of a merger) this does not rule out that this galaxy has had its star formation recently truncated – producing its E+A spectral signature.

5.2 Metallicity gradients

Before we interpret these different radial Hδ slopes further, it is important that we first check whether some of this variation could be owing to metallicity gradients which are well known in galaxies. The strength of the hydrogen Balmer lines depends on the

main-sequence turn-off temperature. Young main-sequence stars are hot and have strong hydrogen absorption. Metal-poor stars also have relatively hot main-sequence stars and stronger hydrogen absorption. However the effect is small compared with the effect of age (Worthey & Ottaviani 1997). Metal absorption lines within the index continuum bands will also affect the derived value of the index. Unfortunately, we cannot attempt a rigorous treatment of metallicity effects for these specific galaxies, because this would require further observation with a broader spectral range and higher signal-to-noise ratios. We can only discuss general trends. The expectation here is that the metallicity decreases with increasing distance from the galactic centre (Searle 1971). There have been various suggestions for the origin of the metallicity gradients in galaxies. The models of Larson (1974); Carlberg (1984) predict that in the process of galaxy formation, the transfer and enrichment of gas toward the galactic centre leads to more metal-enriched stars forming in the central regions and hence the development of a metallicity gradient. Martinelli, Matteucci & Colafrancesco (1998) reproduced the observed metallicity gradients in galaxies using a model in which supernova-driven galactic winds develop first in the outskirts of a galaxy and then successively progress toward the centre.

As the equivalent width of the $H\delta$ line depends on metallicity as well as age, we need to evaluate the effect of a metallicity gradient on the $H\delta_F$ profiles in Fig. 8. We cannot measure the metallicity gradients directly from our spectra because the observed wavelength range does not include a suitable metallicity index. Instead we used the models of Thomas, Maraston & Korn (2004) to compute the effect of metallicity on our measured $H\delta_F$ values. By assuming $[\alpha/Fe]=0$ and a single age population, a linear fit to these models yields the slope

$$\frac{dH\delta_F}{d[Z/H]} \propto -1.98 \ \text{Å}, \tag{9}$$

which is essentially independent of the age of the stellar population. Typical metallicity gradients in early-type galaxies are

$$\frac{d[Z/H]}{d\log r} \propto -0.22 \pm 0.09 \tag{10}$$

(Davies, Sadler & Peletier 1993). We can combine equations (9) and (10) to estimate the radial variation in $H\delta_F$ which would result solely from a gradient in metallicity

$$H\delta_F \propto (0.19 \ \text{Å}) \ln r + \text{constant}. \tag{11}$$

Therefore, typical metallicity gradients in galaxies (in which the metallicity decreases with radius) result in an $H\delta_F$ signature that increases with radius. The radial profiles in Fig. 8 span a range in galactocentric radii of approximately 1–5 kpc; from equation (11), a fractional increase of 31 per cent in $H\delta_F$ over this range would be expected from the metallicity gradient in equation (10), or an average linear slope of 8 per cent kpc^{-1}. In general this is small compared with the size of the observational errors for the E+A galaxies with flat or positive slopes (see Table 2). Of course for those E+A galaxies with negative slopes, a metallicity gradient only serves to diminish this type of radial behaviour; correcting for it would therefore just further steepen the increase in $H\delta$ absorption towards their centres.

5.3 Comparison with numerical models

In order to derive physical meaning from the observed radial gradients of $H\delta_F$ in E+A galaxies, we perform a set of numerical simulations of E+A galaxy formation. We investigate two possible scenarios of E+A galaxy formation: (i) galaxy merging producing strong starbursts (e.g. Z96; Bekki 1998; Bekki et al. 2001); and (ii) abrupt truncation of star formation in disc galaxies (e.g. Poggianti & Barbaro 1996; Shioya, Bekki & Couch 2004).

### 5.3.1 Numerical simulations of $H\delta$ gradients

As the numerical methods and techniques we employ for modelling the chemodynamical and photometric evolution of galaxy mergers and truncated spirals have already been described in detail elsewhere (Bekki & Shioya 1998; Bekki, Shioya & Couch 2001; Bekki, Couch & Shioya 2002), we give only a brief review here.

The progenitor disc galaxies that take part in a merger are taken to have a dark halo, a bulge and a thin exponential disc with a total disc mass (M_d) of $6.0 \times 10^{10} \, M_\odot$ and size (R_d) = 17.5 kpc. We adopt the density distribution of the NFW halo (Navarro, Frenk & White 1996) suggested from CDM simulations and the radial (R) and vertical (Z) density profiles of the disc are assumed to be proportional to $\exp(-R/R_0)$ with scalelength $R_0 = 0.2 \, R_d$, and to $\text{sech}^2(Z/Z_0)$ with scalelength $Z_0 = 0.04 R_d$, respectively. The disc is composed both of gas and stars with a gas mass fraction (f_g) of 0.1. The gas is represented by a collection of discrete gas clouds that follow the observed mass–size relationship. Field star formation is modelled by converting the collisional gas particles into collision-less new stellar particles. We adopt the Schmidt law (Schmidt 1959) with exponent $\gamma = 1.5$ ($1.0 < \gamma < 2.0$, Kennicutt 1998) as the controlling parameter of the rate of star formation. We determined the radial gradient of the $H\delta$ equivalent width for a remnant of a merger scenario (with a prograde–retrograde orbital configuration) at the PSG phase (more than 0.2 Gyr after the peak of the starburst).

For the truncation disc model to be self-consistent we use the same disc parameters as outlined above. The bulge to disc ratio is 0.5. Star formation is *simultaneously and uniformly* truncated throughout the entire disc after $\sim$2 Gyr of isolated evolution (i.e. no tidal interaction/merging and no triggered starbursts). The resulting disc can contain a large fraction of young stars (i.e. A-type stars). Although our assumption of uniform truncation may be oversimplified, particularly in the case of truncation resulting from cluster-related processes such as ram-pressure stripping of disc gas and halo gas stripping, it is adequate for the present study, and serves to illustrate the remarkable differences in the time evolution of $H\delta$ equivalent width radial gradients between the two E+A models (i.e. merger-induced starburst versus truncation).

5.3.2 Comparison with observed $H\delta$ gradients

The simulated $H\delta$ radial profiles for the galaxy merger and instantaneous truncation models are shown in Figs 9 and 10, respectively. For the galaxy merger model in Fig. 9 we overplot the $H\delta_F$ measurements for our three negative-gradient galaxies: CN 254, 22 and 191 (top panel, centre panel and bottom panel, respectively). For the instantaneous truncation model we overplot the observed $H\delta_F$ values of three of our galaxies with positive and flat gradients: CN 849, 247 and 228. In both cases we have displayed the $H\delta_F$ values corrected for convolution with the seeing disc as described in Section 4.3. The errors in the equivalent width measurements after deconvolution were approximated by separately deconvolving the $\pm 1\sigma$ fits to the convolved radial equivalent width profile and comparing the results with the best fit. The observed $H\delta_F$ measurements are plotted as filled squares and the numerical model profiles as solid lines. For the merger model (Fig. 9) we show the radial $H\delta$ gradient
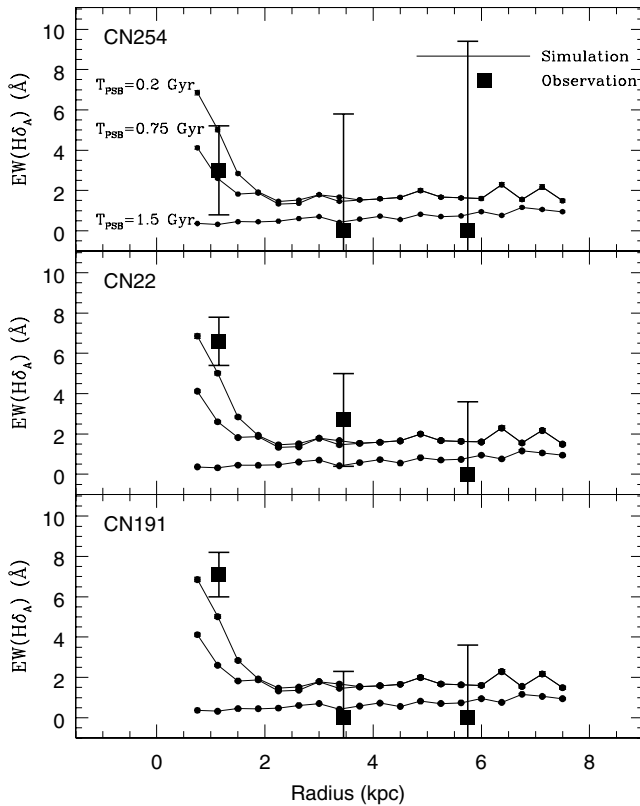
Figure 9. Model Hδ radial profiles for our merger model (solid lines). The model curves are shown with with the observed (deconvolved) Hδ$_F$ data for CN 254 (top panel), CN 22 (middle panel) and CN 191 (lower panel) superimposed as filled squares.

Figure 10. Model Hδ radial profiles for our instantaneous truncation model (solid lines). The model curves are shown with with the observed (deconvolved) Hδ$_F$ data for CN 849 (top panel), CN 247 (middle panel) and CN 228 (lower panel) superimposed as filled squares.

of the merger remnant at times of 0.2, 0.75 and 1.5 Gyr since the maximal starburst. In the case of the instantaneous truncation model displayed in Fig. 10 we show the Hδ profiles at times 0.2, 0.5 and 1.5 Gyr after the truncation of star formation.

It is interesting to compare the differences in the radial behaviour of the Hδ absorption line between the merger and truncation models. In the merger model a centralized burst of star formation is produced, when the starburst ends the galaxy is left with a central population of young stars and hence a radial distribution of Hδ equivalent width which is highest in the centre and decreases rapidly with galactocentric radius (see $T_{PSB} = 0.2$ Gyr profile in Fig. 9). As time progresses after the cessation of star formation the contribution to the integrated light from the youngest stars is diminished, resulting in a decrease in the Hδ equivalent width which causes the radial profile to flatten. At a time $T_{PSB} \approx 1.5$ Gyr after the maximal starburst the radial Hδ profile has evolved to be flat and uniformly low across the entire extent of the galaxy – the E+A galaxy signature is no longer present. The Hδ profiles shown in Fig. 9 are for a major merger model with a specific orbital configuration. However, it is expected that all tidally induced starbursts will exhibit qualitatively similar behaviour, with the star formation concentrated in the galactic centre, producing a PSG spectrum with a radial Hδ equivalent width profile which decreases with galactocentric radius. In contrast, the radial behaviour of the Hδ absorption line in the instantaneous truncation model is quite different. Immediately after the truncation of star formation the galaxy has a flat, uniformly high Hδ equivalent width profile (see $T_{Tr} = 0.2$ Gyr Hδ equivalent width profile in Fig. 10). The galaxy CN 143 exhibits such a profile (compare the radial profile for CN
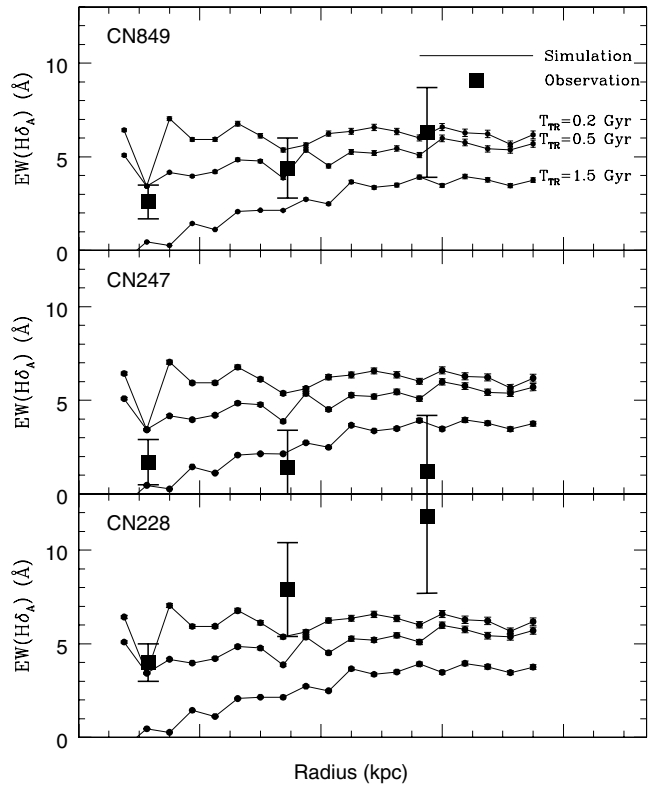
143 in Fig. 8 and $T_{Tr} = 0.2$ Gyr profile in Fig. 10). As the system evolves and the age of the youngest stellar population increases the contribution of the light from this young population of stars decreases. The decrease is most prominent in the centre of the galaxy where there exists a larger fraction of old stars; this results in the Hδ equivalent width decreasing most rapidly in the central regions of the galaxy, leading to a positive Hδ equivalent width gradient which steepens with time.

Given the very different expectations for the behaviour and time evolution of the Hδ equivalent width radial profile in E+A galaxies for the two formation mechanisms discussed (i.e. merger-induced starbursts and abrupt truncation of star formation) we propose that the radial distribution of Hδ absorption in E+A galaxies provides a useful tool in differentiating between these two formation mechanisms. In the sample of eight E+A galaxies examined here we find three galaxies (CN 254, 22 and 191) which have a negative Hδ$_F$ gradient. We suggest that this radial behaviour provides evidence that the E+A spectral signature in these galaxies has its origin in a merger or tidal interaction. The remaining five E+A galaxies (CN 143, 89, 849, 228 and 247) have either flat or radially increasing Hδ$_F$ profiles, these profiles are more consistent with the recent truncation of star formation in normal disc galaxies.

6 SUMMARY

We have obtained IFU spectra for 12 galaxies in AC 114 originally classified as E+A systems by CS87, permitting the first investigation of the spatial distribution of Hδ absorption in such galaxies. We summarize our findings as follows.

(i) We find global Hδ equivalent width values lower than in the original CS87 sample from which our targets were selected. This is especially the case for the five galaxies which were original assigned an HDS classification by CS87. We attribute this to differences in aperture placement and/or systematic errors in the sky subtraction of the original CS87 sample. Some galaxies appear to have been misclassified based on the original CS87 spectroscopy.

(ii) Three galaxies in our sample exhibit negative $H\delta_F$ gradients implying a strong central concentration of young stars. The E+A galaxies in our sample which exhibit this property are CN 254, 22 and 191. Normal metallicity gradients in galaxies, in which metallicity decreases with galactic radius, would imply an even more significant central concentration, as does correction for the smearing of the galaxy light owing to seeing. The distribution of young star light in these galaxies is consistent with the origin of the global E+A signature being the result of a merger or tidal interaction.

(iii) Three galaxies in the sample, CN 143, 89 and 247 (which has globally low $H\delta_F$) have a $H\delta_F$ profile which is statistically consistent with being flat. This profile is consistent with a galaxy observed shortly after the global truncation of its star formation.

(iv) Two galaxies in the sample show a positive $H\delta_F$ gradient with Hδ absorption being at its weakest at the centre of the galaxy. The galaxies in this category are CN 89 and 228. These $H\delta_F$ profiles are consistent with a galaxy which has undergone a global truncation of its star formation within the last 2 Gyr.

ACKNOWLEDGMENTS

REFERENCES

Abazajian K. et al., 2004, AJ, 128, 502
Abell G. O., Corwin H. G., Olowin R. P., 1989, ApJS, 70, 1
Balogh M. L., Morris S. L., Yee H. K. C., Carlberg R. G., Ellingson E., 1999, ApJ, 527, 54
Barger A. J., Aragon-Salamanca A., Ellis R. S., Couch W. J., Smail I., Sharples R. M., 1996, MNRAS, 279, 1
Bartholomew L. J., Rose J. A., Gaba A. E., Caldwell N., 2001, AJ, 122, 2913
Bekki K., 1998, ApJ, 502, L133
Bekki K., 1999, ApJ, 510, L15
Bekki K., Shioya Y., 1998, ApJ, 497, 108
Bekki K., Shioya Y., Couch W. J., 2001, ApJ, 547, L17
Bekki K., Couch W. J., Shioya Y., 2002, ApJ, 577, 651
Blake C. et al., 2004, MNRAS, 355, 713
Bruzual G., Charlot S., 2003, MNRAS, 344, 1000
Cardiel N., Gorgas J., Cenarro J., Gonzalez J. J., 1998, A&AS, 127, 597
Carlberg R. G., 1984, ApJ, 286, 403
Colless M. et al., 2001, MNRAS, 328, 1039
Couch W. J., 1981, PhD thesis, Australian National Univ.
Couch W. J., Newell E. B., 1984, ApJS, 56, 143
Couch W. J., Sharples R. M., 1987, MNRAS, 229, 423
Couch W. J., Ellis R. S., Sharples R. M., Smail I., 1994, ApJ, 430, 121
Couch W. J., Barger A. J., Smail I., Ellis R. S., Sharples R. M., 1998, ApJ, 497, 188
Davies R. L., Sadler E. M., Peletier R. F., 1993, MNRAS, 262, 650
De Filippis E., Bautz M. W., Sereno M., Garmire G. P., 2004, ApJ, 611, 164
Dressler A., Gunn J. E., 1983, ApJ, 270, 7
Dressler A., Gunn J. E., 1992, ApJS, 78, 1
Dressler A., Smail I., Poggianti B. M., Butcher H., Couch W. J., Ellis R. S., Oemler A. J., 1999, ApJS, 122, 51
Fabricant D. G., McClintock J. E., Bautz M. W., 1991, ApJ, 381, 33
Franx M., 1993, ApJ, 407, L5
Goto T., 2005, MNRAS, 357, 937
Gunn J. E., Gott J. R. I., 1972, ApJ, 176, 1
Kennicutt R. C., 1998, ApJ, 498, 541
Larson R. B., 1974, MNRAS, 166, 585
Mahdavi A., Geller M. J., 2001, ApJ, 554, L129
Martinelli A., Matteucci F., Colafrancesco S., 1998, MNRAS, 298, 42
Mihos J. C., Hernquist L., 1996, ApJ, 464, 641
Moore B., Lake G., Katz N., 1998, ApJ, 495, 139
Navarro J. F., Frenk C. S., White S. D. M., 1996, ApJ, 462, 563
Norton S. A., Gebhardt K., Zabludoff A. I., Zaritsky D., 2001, ApJ, 557, 150
Poggianti B. M., Barbaro G., 1996, A&A, 314, 379
Poggianti B. M., Smail I., Dressler A., Couch W. J., Barger A. J., Butcher H., Ellis R. S., Oemler A. J., 1999, ApJ, 518, 576
Rose J. A., Gaba A. E., Caldwell N., Chaboyer B., 2001, AJ, 121, 793
Salpeter E. E., 1955, ApJ, 121, 161
Schmidt M., 1959, ApJ, 129, 243
Searle L., 1971, ApJ, 168, 327
Shioya Y., Bekki K., Couch W. J., 2004, ApJ, 601, 654
Thomas D., Maraston C., Korn A., 2004, MNRAS, 351, L19
Tonry J., Davis M., 1979, AJ, 84, 1511
Vazdekis A., 1999, ApJ, 513, 224
Wild V. et al., 2005, MNRAS, 356, 247
Worthey G., Ottaviani D. L., 1997, ApJS, 111, 377
Yang Y., Zabludoff A. I., Zaritsky D., Lauer T. R., Mihos J. C., 2004, ApJ, 607, 258

This paper has been typeset from a TeX/LaTeX file prepared by the author.